Stress-based forecasting of induced seismicity with instantaneous earthquake failure functions: Applications to the Groningen Gas Reservoir.

Jonathan D. Smith[1], Elías R. Heimisson[1,2], Stephen J. Bourne[3], Jean-Philippe Avouac.[1]

Abstract

In this study we use the Groningen gas field to test a new method to assess stress changes due to gas extraction and forecast induced seismicity. We take advantage of the detailed knowledge of the reservoir geometry and production history, and of the availability of surface subsidence measurements and high quality seismicity data. The subsurface is represented as a homogeneous isotropic linear poroelastic half-space subject to stress changes in three-dimensional space due to reservoir compaction and pore pressure variations. The reservoir is represented with cuboidal strain volumes. Stress changes within and outside the reservoir are calculated using a convolution with semi-analytical Green functions. The uniaxial compressibility of the reservoir is spatially variable and constrained with surface subsidence data. We calculate stress changes since the onset of gas production. Coulomb stress changes are maximum near the top and bottom of the reservoir where the reservoir is offset by faults. To assess earthquake probability, we use the standard Mohr-Coulomb failure criterion assuming instantaneous nucleation and a non-critical initial stress. The distribution of initial strength excess, the difference between the initial Coulomb stress and the critical Coulomb stress at failure, is treated as a stochastic variable and estimated

*Corresponding author: avouac@gps.caltech.edu
[1]Division of Geological and Planetary Sciences, California Institute of Technology, Pasadena, 91106, California, USA.
[2]Swiss Seismological Service, ETH Zurich, Zurich, Switzerland
[3]Shell Global Solutions, Amsterdam, Netherlands

from the observations and the modelled stress changes. The exponential rise of seismicity nearly 30 years after the onset of production, provides constraints on the distribution of initial strength. The lag and exponential onset of seismicity are well reproduced assuming either a generalized Pareto distribution, which can represent the tail of any distribution, or a Gaussian distribution, to describe both the tail and body of the distribution. The Gaussian distribution allows to test if the induced seismicity at Groningen has transitioned to the steady-state where seismicity rate is proportional to the stressing rate. We find no evidence that the system has reached such a steady-state regime. The modeling framework is computationally efficient making it possible to test the sensitivity to modeling assumptions regarding the estimation of stress changes. The forecast is found robust to uncertainties about the ability of the model to represent accurately the physical processes. It does not require in particular a priori knowledge of the location and orientation of the faults that can be activated. The method presented here is in principle applicable to induced seismicity in any setting provided deformation and seismicity data are available to calibrate the model.

Keywords: Induced Seismicity, Probabilistic Forecasting, Reservoir Deformation

---

1. Introduction

The Groningen gas field, situated in the north-east of the Netherlands (Figure 1), has been in production since 1963. Prior to gas extraction, no historical earthquakes had been reported in the area (Dost et al., 2017). Starting in the 1990*s* small magnitude earthquakes have been detected, with some of these shallow events causing non-structural damage and public concern (Figure 1; Dost et al., 2017). As a result, it was decided to reduce production from 2014 on (van der Molen et al., 2019). The concern caused by induced seismicity at Groningen has prompted large efforts to monitor the seismicity and surface deformation induced by the reservoir compaction and to develop quantitative

models of the seismicity response to the reservoir operations (e.g. Bourne and Oates, 2017; Bourne et al., 2018; Dempsey and Suckale, 2017; Dost et al., 2017, 2020; Richter et al., 2020).

In this study we take advantage of this rich dataset to explore different modeling strategies to forecast induced seismicity. We follow the well established paradigm that seismicity is driven by Coulomb stress changes (King et al., 1994), a view already adopted in previous studies of induced seismicity at Groningen (Bourne and Oates, 2017; Bourne et al., 2018; Dempsey and Suckale, 2017; Richter et al., 2020). We test different strategies to assess stress changes, taking advantage of a refined model of reservoir compaction constrained from production data and from surface deformation measurements (Smith et al., 2019). We additionally assume that the lag of seismicity is due to the fact that faults in this stable tectonic area where not critically stressed initially (Bourne and Oates, 2017; Bourne et al., 2018). Assuming the standard Mohr-Coulomb failure model, an earthquake nucleates when the Coulomb stress on a fault reaches a critical value that represent the fault strength. In this context the seismicity evolution depends on the shape of the function representing the distribution of excess strength, the difference between the initial stress and the critical stress at failure. We test whether the time evolution of seismicity reflects only the tail of that distribution, as assumed in the extreme threshold failure model (Bourne and Oates, 2017; Bourne et al., 2018) which explains well the initial exponential rise of seismicity, or whether it shows a transition to the steady-state regime where seismicity should be proportional to stress rate. Dempsey and Suckale (2017) were able to forecast satisfactorily the time-evolution of seismicity assuming such a steady-state regime but didn't model how it was established.
Here, we treat earthquake nucleation as instantaneous. The nucleation process is in fact not instantaneous and this feature, which can be accounted for using the rate-and-state friction formalism (Dieterich, 1994), could explain the seismicity lag (Candela et al., 2019). We assess the effect of non-instantaneous earthquake nucleation in another study (Heimisson et al., 2021). The forecasting performance can been further improved with a more sophisticated representa-

tion of earthquake nucleation, but the assumption of an instantaneous failure is an appropriate approximation to forecast seismicity at the annual to multi-annual time-scale considered here.

2. Stress changes due to pore pressure variations and reservoir compaction

2.1. Principle of our approach and comparison with previous approaches

To estimate the probability of fault failure, we need to model the stress redistribution due to the reservoir compaction and pore pressure variations within and outside the reservoir with account for poroelastic effects (Wang, 2018). The geometry of the reservoir is well known from various geophysical investigations (seismic reflection and seismic refraction), borehole core samples and logging data. The reservoir lies at a depth varying between 2.6 and 3.2km, with a thickness increasing northeastward from about 100m to 300m. Numerous faults are offsetting the reservoir (Figure 1) with throws exceeding the reservoir thickness at places. Pressure depletion lead to compaction of the reservoir, shear stress build up on these faults and deformation of the surrounding medium.
Various approaches have been used in past studies to calculate the resulting stress redistribution. Some have adopted a simplified model to enable forecasting seismicity at the scale of the entire reservoir as we do in this study. Dempsey and Suckale (2017) proposed a forecasting scheme which accounts for the effect of the local pore pressure change on poroelastic stress changes. They ignore reservoir heterogeneities and assume that the earthquakes occur within the reservoir. These model assumptions are questionable. The distribution of hypocenter depth, which were determined with an uncertainty of 500m taking into account heterogeneities of seismic velocities (Smith et al., 2020), suggests that earthquake nucleate within the reservoir (28%) or in the overburden (60%), with the mode of the distribution peaking at the depth of the reservoir caprock. In addition, the earthquakes should tend to occur in zones of stress concentration

induced by spatial variations of the the reservoir properties. Bourne et al. (2018) developed a semi-analytical reservoir depth integrated model which is also limited to the estimate of stress changes within the reservoir itself, but account for stress concentration at the faults offsetting the reservoir. The faults characteristics are not represented in any detail though, and the reservoir compressibility is assumed uniform. Some other studies have used approaches that allow for a more detailed representation of stress concentration at the faults offsetting the reservoir and for the assessment of stress changes within and outside the reservoir. In particular, Jansen et al. (2019) used a two-dimensional closed-form analytical expressions to investigate stress redistribution and the possibility of reactivating faults with any geometry. Other authors have carried out similar investigations using two-dimensional finite-element simulations (Mulders, 2003; Rutqvist et al., 2016; Buijze et al., 2017, 2019). It provided important insight on the mechanics of fault reactivation, but the methods used in these studies to estimate stress redistribution can't be easily included in a seismicity forecasting scheme at the large scale of the reservoir due to the need to consider 3-D effects and the computational cost. Finally, some authors have adopted a simplified representation of the deforming reservoir as a series of point sources of strain (van Wees et al., 2019; Candela et al., 2019). This approach is efficient as the Green Functions are analytical. It allows to calculate stress changes in the 3-D volume and can feed a seismicity forecasting scheme easily. It however suffers from the fact that it is very sensitive to the number and distribution of point sources representing the reservoir and to the distribution of the receiver points where stress changes are evaluated. This issue is inherent to the point source representation due to the stress singularity at the source location.

We also use a Green function approach but adopt a strain volume formulation (Kuvshinov, 2008) rather than a point source formulation. The deforming reservoir is represented as a series of cuboidal volumes which are deforming poroelastically. We adopted a cuboidal elementary volumes as it is an efficient way to represent, to the first order, spatial variations of the reservoir geometry, due in particular to the faults offsetting the reservoir. These faults are represented

as vertical faults but the method could be expanded to account for any fault dip angles using more general polyhedral elementary volumes. The displacement and stress Green's functions for polyhedral volumes are semi-analytical and therefore easy to compute (Kuvshinov, 2008). This approach has the additional benefit that the method makes it easy to compute the stress changes for any production scenario by the convolution of the Green's functions with the evolving pressure field. This is an appreciable feature for earthquake forecasting, eventually applicable in real-time. A difference between our approach and that of Candela et al. (2019), in addition to the strain volume instead of the point formulation, is that we assume that earthquakes can occur on unmapped faults. We therefore don't restrict the stress calculations to the set of known faults. The advantage is that our approach doesn't require any prior knowledge of the faults that could be reactivated.

2.2. Implementation of the strain-volume model

We use the pressure depletion model developed by the operator, MoReS (Nederlandse Aardolie Maatschappij, 2013), which was generated from history matching using the production rates, pressure gauge measurements, flow gauge measurements, and tracer timing measurements.

Surface subsidence over the gas field has been well documented with different geodetic and remote sensing techniques including optical levelling, persistent scatterer interferometric synthetic aperture radar (PS-InSAR) and continuous GPS (cGPS). Smith et al. (2019) combined all these data to describe the evolution of surface subsidence and the related reservoir compaction from the start of gas production until 2017. They additionally used the pressure depletion model of Nederlandse Aardolie Maatschappij (2013) to determine the spatially variable compressibility of the reservoir. Since the lateral extent of the reservoir ($\sim 40 \times 40$km) is much greater than the reservoir thickness ($100 - 300$m), the reservoir pressure depletion at any map point can be related to the reservoir

compaction by:

$$C = hC_m\Delta P \tag{1}$$

where C is the compaction of the reservoir, C_m the uniaxial compressibility, ΔP the pressure depletion and h the reservoir thickness. The uniaxial compressibility was determined based on the pressure depletion from MoReS, the reservoir thickness, and the reservoir compaction (Smith et al., 2019). Kuvshinov (2008) determined the semi-analytical Green functions relating compaction of a cuboid to surface subsidence by integration of the nucleus of strain solution (Geertsma, 1973) over the cuboid volume assumed to be isotropic and homogeneous. Dyskin et al. (2020) recently questioned the validity of Geerstma's solution based on the fact that the subsidence is always smaller than the reservoir compaction by a factor $2(1-\nu)$ even if the reservoir is assumed of large horizontal extent compared to its depth. This paradox is discussed by Kuvshinov (2007) who demonstrates that this factor is due to the uplift of the reservoir bottom. The Green function of Dyskin et al. (2020) for a nuclei of strain may however have a merit in the case of a very stiff underburden compared to the reservoir and could be used as a alternative to Geerstma's solution which assumes a homogeneous elastic half space.mKuvshinov (2008)'s formulation depends on the relative position of the vertices defining each cuboid (i) relative to the observation point, $\vec{x} = (x, y, z)$,

$$\bar{x}_{(i)} = x_{(i)} - x, \tag{2}$$

$$\bar{y}_{(i)} = y_{(i)} - y, \tag{3}$$

$$\zeta^{\pm} = z_{(i)} \mp z, \tag{4}$$

where $x_{(i)}$, $y_{(i)}$ and $z_{(i)}$ are the location for each vertex. The displacement, $U = (U_x, U_y, U_z)$, at an observation point at the free surface, $Z = 0$, due to a

given cuboid is determined from the summation over all its vertices with

$$U_x = \frac{\alpha C_m \Delta P}{4\pi} \sum_{\text{vertices}} (-1)^{i-1} \left[f\left(\bar{y}, \zeta_-, \bar{x}, R_-\right) + (3-4\nu)\, f\left(\bar{y}, \zeta_+, \bar{x}, R_+\right) + 2 \cdot z \ln\left(|R_+ \bar{y}|\right) \right], \tag{5}$$

$$U_y = \frac{\alpha C_m \Delta P}{4\pi} \sum_{\text{vertices}} (-1)^{i-1} \left[f\left(\bar{x}, \zeta_-, \bar{y}, R_-\right) + (3-4\nu)\, f\left(\bar{x}, \zeta_+, \bar{y}, R_+\right) + 2z \cdot \ln\left(|R_+ + \bar{x}|\right) \right], \tag{6}$$

$$U_z = -\frac{\alpha C_m \Delta P}{4\pi} \sum_{\text{vertices}} (-1)^{i-1} \left[f\left(\bar{x}, \bar{y}, \zeta_-, R_-\right) + (3-4\nu)\, f\left(\bar{x}, \bar{y}, \zeta_+, R_+\right) - 2z \cdot \operatorname{atan}\left(\frac{\zeta_+ R_+}{\bar{x}\bar{y}}\right) \right], \tag{7}$$

where $R^{\pm} = \sqrt{\bar{x}^2 + \bar{y}^2 + \left(\zeta^{\pm}\right)^2}$ and

$$f\left(x, y, Z, R\right) = Z \cdot \operatorname{atan}\left(\frac{xy}{ZR}\right) - x \ln\left(|R+y|\right) - y \ln\left(|R+x|\right). \tag{8}$$

Following Smith et al. (2019) we represent the reservoir with cuboids of 500m × 500m horizontal dimension. The depth and height of each cuboid is set to the average depth and thickness of the reservoir over this 500 × 500m area.

Smith et al. (2019) found that the uniaxial compressibility is pressure invariant and determine spatial variations of compressibility with a resolution approximately 3km. Smaller-scale spatial variations of compaction, and hence of compressibility, cannot be derived from surface deformation due to the depth of the reservoir. As such the uniaxial compressibility model can be considered as a smoothed representation of the reservoir compressibility. Downstream applications of this model for stress calculations, Coulomb stress and earthquake forecasting should be smoothed to the same 3km resolution.

Given that earthquake might nucleate within the reservoir, possibly in the underburden, or more probably in the overburden (Smith et al., 2020), the stress changes are evaluated both within, and outside the reservoir. We assume no pore pressure depletion outside the reservoir.

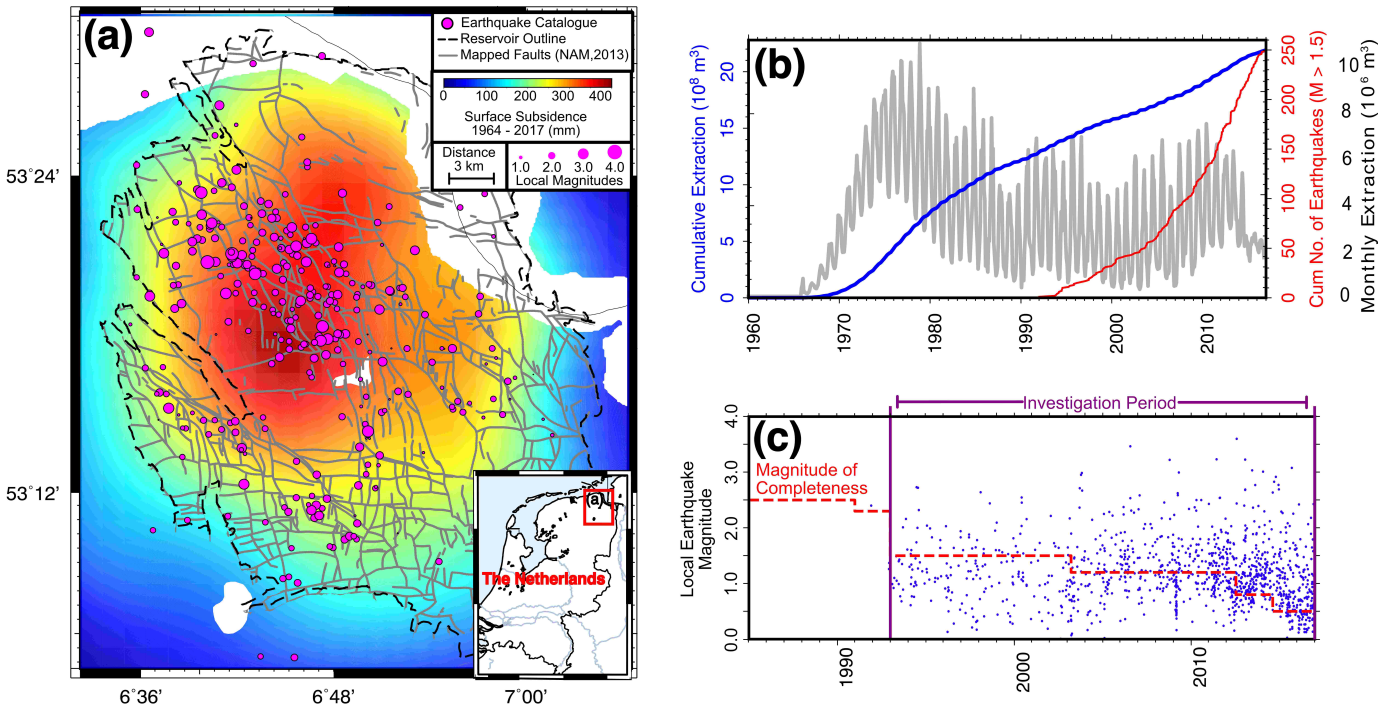

Figure 1: Relationships between surface subsidence, seismicity and cumulative extraction. (a) Surface subsidence and seismicity (pink circles with size proportional to magnitude) from 1964 to 2017 (Smith et al., 2019). The maximum magnitude over the period is $M_L = 3.6$). The black dashed line shows the extent of the gas reservoir. (b) Cumulated extracted gas volume, monthly extracted volumes, and cumulative number of earthquakes as a function of time. (c) Earthquake magnitude from 1985 to 2017. Red dashed line show magnitude of completeness. Purple lines show the time period under investigation in this article.

The stress changes are calculated with Kuvshinov (2008) solution with the convention that normal stress is positive in compression,

$$\begin{aligned}\sigma_{xx} =&\frac{\alpha C_m G\Delta P}{2\pi}\sum_{\text{vertices}}(-1)^{i-1}\left[-\text{atan}\left(\frac{\bar{x}R_-}{\bar{y}\zeta_-}\right)-(3-4\nu)\,\text{atan}\left(\frac{\bar{x}R_+}{\bar{y}\zeta_+}\right)\right.\\&\left.+4\nu\cdot\text{atan}\left(\frac{\zeta_+R_+}{\bar{x}\bar{y}}\right)-\frac{2\bar{x}\bar{y}z}{R_+\left(\bar{x}^2+\zeta_+^2\right)}\right],\end{aligned}\tag{9}$$

$$\begin{aligned}\sigma_{yy} =&\frac{\alpha C_m G\Delta P}{2\pi}\sum_{\text{vertices}}(-1)^{i-1}\left[-\text{atan}\left(\frac{\bar{y}R_-}{\bar{x}\zeta_-}\right)-(3-4\nu)\,\text{atan}\left(\frac{\bar{y}R_+}{\bar{x}\zeta_+}\right)\right.\\&\left.+4\nu\cdot\text{atan}\left(\frac{\zeta_+R_+}{\bar{x}\bar{y}}\right)-\frac{2\bar{x}\bar{y}z}{R_+\left(\bar{y}^2+\zeta_+^2\right)}\right],\end{aligned}\tag{10}$$

$$\begin{aligned}\sigma_{zz} =&-\frac{\alpha C_m G\Delta P}{2\pi}\sum_{\text{vertices}}(-1)^{i-1}\left[-\text{atan}\left(\frac{\zeta_-R_-}{\bar{x}\bar{y}}\right)+\text{atan}\left(\frac{\zeta_+R_+}{\bar{x}\bar{y}}\right)\right.\\&\left.-\frac{2\bar{x}\bar{y}z}{R_+}\left(\frac{1}{\bar{x}^2+\zeta_+^2}+\frac{1}{\bar{y}^2+\zeta_+^2}\right)\right],\end{aligned}\tag{11}$$

$$\begin{aligned}\sigma_{xy} =&-\frac{\alpha C_m G\Delta P}{2\pi}\sum_{\text{vertices}}(-1)^{i-1}\left[\ln\left(|R_-+\zeta_-|\right)\right.\\&\left.+(3-4\nu)\ln\left(|R_++\zeta_+|\right)-\frac{2z}{R_+}\right],\end{aligned}\tag{12}$$

$$\begin{aligned}\sigma_{xz} =&\frac{\alpha C_m G\Delta P}{2\pi}\sum_{\text{vertices}}(-1)^{i-1}\left[\ln\left(\left|\frac{R_-+\bar{y}}{R_++\bar{y}}\right|\right)\right.\\&\left.-\frac{2z\bar{y}\zeta_+}{R_+\left(\bar{x}^2+\zeta_p^2\right)}\right],\end{aligned}\tag{13}$$

$$\begin{aligned}\sigma_{yz} =&-\frac{\alpha C_m G\Delta P}{2\pi}\sum_{\text{vertices}}(-1)^{i-1}\left[\ln\left(\left|\frac{R_-+\bar{x}}{R_++\bar{x}}\right|\right)\right.\\&\left.-\frac{2z\bar{x}\zeta_+}{R_+\left(\bar{y}^2+\zeta_p^2\right)}\right].\end{aligned}\tag{14}$$

All model parameters are listed in Table 1. The Biot coefficient is in particular set to $\alpha = 1.0$. Due to poroelasticity, the pressure depletion leads to a decrease of the horizontal stress. For a reservoir of large horizontal extent compared to its depth this effect is characterized by the stress path coefficient

Parameter	***Value***
Biot's Coefficient Alpha	1.0
Coefficient of Friction	0.66
Poisson Ratio	0.25
Shear Modulus	6GPa

Table 1: Parameters used in the calculation of stress changes induced by pressure changes in the reservoir using the strain volume formulation

$A = \frac{\Delta\sigma_h}{\Delta P} = \alpha\frac{1-2\nu}{1-\nu}$. Because the vertical stress is determined by the overburden, it remains constant during gas extraction if the mass of the extracted gas is neglected. It results that the stress path is an important parameters which determines stress changes in the reservoir (Hettema et al., 2000). Given the value of the Poisson coefficient, $\nu = 0.25$, the stress path coefficient corresponding to our model parameters is $A = 0.66$. For comparison, field measurements have indicated $A = 0.4 \pm 0.2$ and laboratory measurements have yielded values between 0.7 and 0.8 (Hettema et al., 2000; Hol et al., 2018). The displacement and stress fields for a single cuboid is shown in Supplementary Figure A1. The cross-section is taken along the y-axis in the centre of the cuboid. Note the stress localization at the edges of the cuboid. The free surface has little effect in he case of a single cuboid due to its small size compared to the reservoir depth.

The point of failure of an intact rock or of reactivation of an existing fault is commonly assessed using the Mohr-Coulomb failure criterion (Handin, 1969). A number of studies have also demonstrated that this criterion can be used effectively to assess earthquake triggering by stress changes (e.g. King et al., 1994). According to this criterion failure occurs when the shear-stress τ exceeds the shear-strength of the material τ_f, which depends on the effective normal stress, $\sigma_n' = \sigma_n - \Delta_P$, according to

$$\tau_f = \mu(\sigma_n - P) + C_0, \tag{15}$$

where τ_f is shear-stress, σ_n is the normal-stress (positive in compression), P is the pore pressure, μ is the internal friction and C_0 is the cohesive strength. If the material is not at failure the strength excess is $\tau_f - \tau$. Pressure changes play an important role in preventing or promoting fault failure. Assuming the total stresses do not change, a greater pore pressure acts to lower the effective normal stress and promotes failure. By contrast, a pressure decrease should inhibit failure. It is customary to assess jointly the effect of stress changes and pore pressure changes using the Coulomb stress change defined as

$$\Delta C = \Delta\tau + \mu(\Delta P - \Delta\sigma_n), \tag{16}$$

where ΔC is the change in Coulomb stress, $\Delta\tau$ is the shear stress change, μ is the internal friction, $\Delta\sigma_n$ is the change in normal stress, and ΔP is the change in pore pressure.

A cross-section of the displacement and stress calculated with our representation of the reservoir as a series of cuboids is shown in Figure 2. The figure also shows the 'maximum Coulomb stress change', defined as the maximum Coulomb stress change for all possible faults orientation, and a 'fault Coulomb stress change' defined as the Coulomb stress change on faults with a fixed orientation. The rose diagram of faults orientation (Figure A2) shows two dominant modes corresponding to strikes of N270^{o}E and N350^{o}E. Dip angles are steep typically around 85^o (Nederlandse Aardolie Maatschappij, 2013). We consider one or the other fault orientation. The choice of any fixed orientation result in fact in only a rescaling of the Coulomb stress changes. The Coulomb stress changes are largest at the top or bottom of the reservoir in the vicinity of the most prominent reservoir discontinuities. The stress concentrations at the edges of the cuboids interfere destructively where there are no offsets between adjacent cuboids.

A striking feature of our model is that the Coulomb stress change is mostly negative within the reservoir. Within the reservoir, the pore pressure the poroelastic

effect can outweigh the pressure decrease and this effect has been considered to be major cause for the seismicity at Groningen. In fact, considering a 1-D reservoir model and the dependence on the effective normal stress $\sigma'_n = \sigma_n - \Delta_P$, the Coulomb stress can increase for a decrease of the pore pressure only if the Biot-coefficient, $A = \alpha\frac{1-2\nu}{1-\nu}$, exceeds a critical values which depends on the on the internal friction angle ϕ and Poisson coefficient ν,

$$\alpha_c = \frac{1-\nu}{1-2\nu}\frac{2\sin\phi}{1+\sin\phi}. \tag{17}$$

With the standard parameters we have chosen (Table 1), $\alpha_c = 1.07$ so that the poroelastic effect in the reservoir cannot in principle exceeds the effect the pressure drop since the Biot coefficient cannot exceed 1. A combination of a small Poisson coefficient, a large Biot coefficient and low internal friction is needed. This happens with the parameters used by Buijze et al. (2019) who assumed a Poisson coefficient of 0.15, a friction of 0.6 and Biot coefficient 1.0. The critical value of the Biot coefficient is 0.83 in that case. We verified this by calculating the stress changes at the center of a reservoir of large spatial extent (see supplementary Figure A6).

The calculation using the cuboid approach is very efficient. For example,it takes 60s to calculate the cross-section presented in Figure 2 on a standard desktop computer with the code supplied in the Google Colab notebook. This section is composed of 8174 receiver points at 15m spacing in X and Z dimensions, computed from the convolution with the 8174 cuboids.

2.3. Comparison with other models of stress changes

We compare our results with the stress change calculations presented by Candela et al. (2019) and to those obtained with the Elastic Thin-Sheet (ETS) approximation of Bourne and Oates (2017).

Candela et al. (2019) calculated the maximum Coulomb stress changes on faults offsetting the reservoir using the 3-D model MACRIS (van Wees et al.,

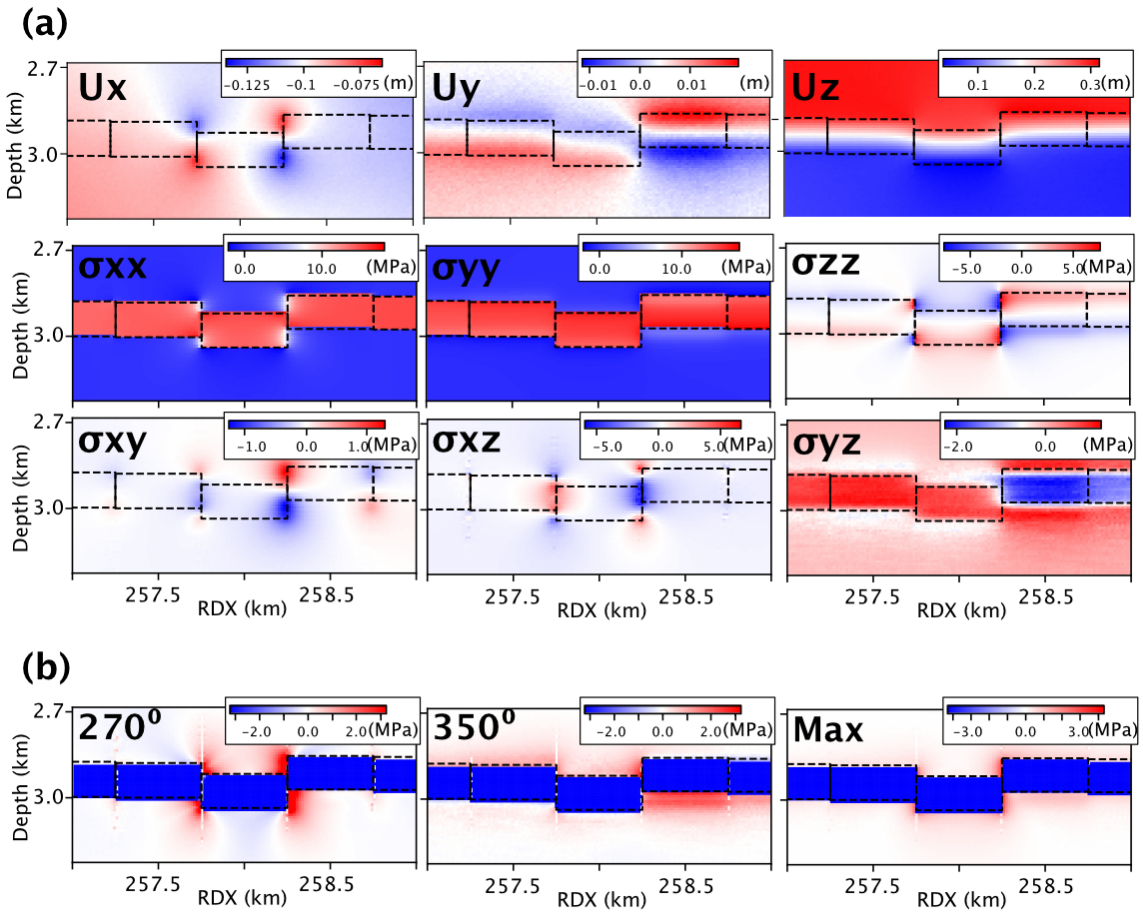

Figure 2: (a) Displacement (U in m), and stress tensor components (σ in MPa) along a vertical cross-section through a series of cuboids representing the simplified geometry of the depleting reservoir (black dashed lines). (b) Maximum Coulomb stress and fault Coulomb stress (MPa) calculated for a fault orientation corresponding to the regional average strike directions (270^o and 350^o), and dip (85^o) angles.

2019). Their calculation shows an overall pattern and amplitudes of stress changes similar to the stress changes calculated with our model near the edges of the cuboids (Figure 3). Note that our calculation cannot be made exactly at the the edges within the reservoir because the mathematical singularity. The values are therefore very sensitive to the choice of the exact point of sampling. Similarly the output from MACRIS is very sensitive to the exact location of the point sources with respect to the faults. The comparison between the two models can therefore only be qualitative. Sampling our model near the cuboid edges exaggerates the fractional area of high stress change because the peak value is assigned to the entire sampling cell. If the calculation is made in the caprock above the reservoir, the stress changes are very sensitive to the distance from the top of the reservoir if sampled above the edges of the cuboids. The stress change calculated at the grid points above the centers of the cuboids are more stable, although much smaller (Figure 3) but probably more representative of the stress change with the sampling cell.

In the ETS formulation, the vertical averaged strain of a reservoir with spatially varying thickness $h(x, y)$ is expressed a function of the vertical strain, ε_{zz} and reservoir depth, z_0 according to,

$$\bar{\varepsilon_{xz}} = -\frac{\varepsilon_{zz}}{2}\frac{\partial z_0}{\partial x} + \frac{h}{4}\frac{\partial \varepsilon_{zz}}{\partial x}, \tag{18}$$

$$\bar{\varepsilon_{yz}} = -\frac{\varepsilon_{zz}}{2}\frac{\partial z_0}{\partial y} + \frac{h}{4}\frac{\partial \varepsilon_{zz}}{\partial y}, \tag{19}$$

$$\bar{\varepsilon_{zz}} = \varepsilon_{zz}. \tag{20}$$

In the ETS formulation the distribution of earthquakes in time and space is derived from the deformation of the reservoir due to uniaxial compaction and to the associated vertical shear strain resulting from the spatial variations of the reservoir elevation and thickness. It accounts for the effect of poroelasticity and for shear at the faults offsetting the reservoir. The earthquakes are assumed to occur only within the reservoir. For consistency with the study of Bourne

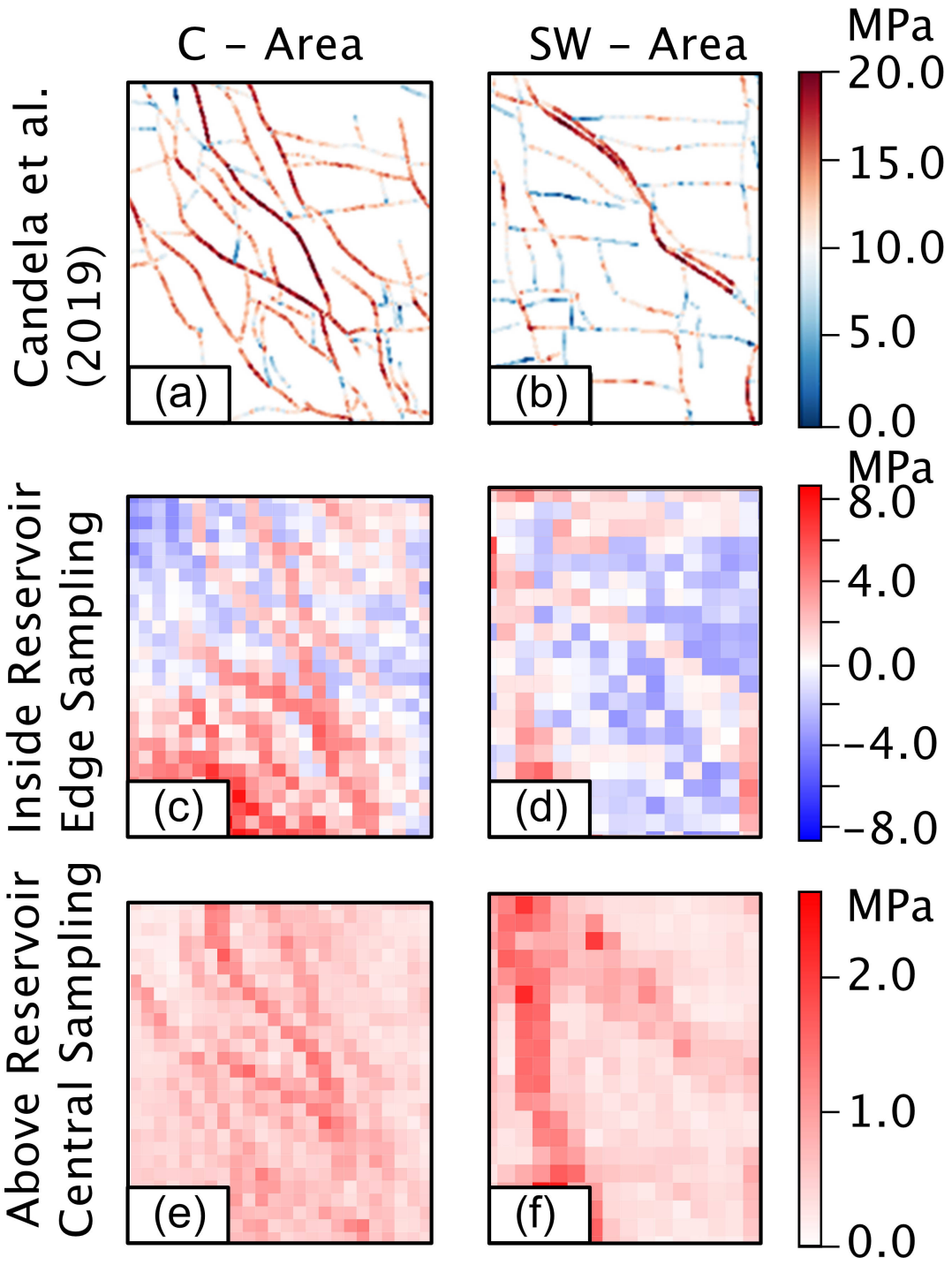

Figure 3: Coulomb stress changes between 1965 and 2016 for two regions in South-West (a) and Central (b) part of the reservoir from Candela et al. (2019). The plots shows the maximum Coulomb stress change on the known faults in these areas. Maximum Coulomb stress change calculated with our model in the reservoir near the cuboid edges (c,d), 10 m away in the E and N direction from the north east corner of each cuboid, or in the caprock (e,f), 5m above the top of the reservoir and above the centers of the cuboids.

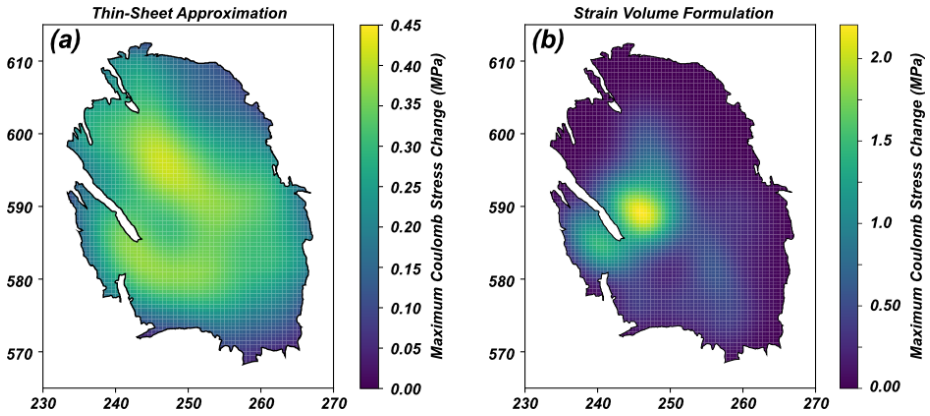

Figure 4: Comparison of the Thin-Sheet Bourne and Oates (2017) and Strain-Volume maximum Coulomb stress change for the period of 1965-2017. (a) Thin-sheet maximum Coulomb stress change with black outline representing the reservoir outline at depth (b) Strain volume maximum Coulomb stress change calculated within the reservoir at the North-East of the cell blocks, smoothed to 3.2km resolution

and Oates (2017), the calculation is made with a Poisson Coefficient $\nu = 0.2$, a friction angle $\phi = 0.5$ and a Biot coefficient = 1. In that case, failure is promoted both by the shear induced by the reservoir geometry and by the poroelastic increase of differential stress. In their implementation Bourne and Oates (2017) applied a spatial smoothing and filter out faults with offset exceeding some given fraction of the reservoir thickness offset. The two parameters, optimized to best fit the seismicity data using a Markov-Chain Monte Carlo procedure, were determined as 3.2km and 0.43 respectively. Thresholding faults with large offset relative to the reservoir thickness is justified by the presence of salt above the anhydrite caprock. Faults with large offset presumably juxtapose the reservoir against the salt and could be considered aseismic. The pattern of stress Coulomb changes within the reservoir, sampled near the cuboid edges and smoothed with the same Gaussian kernel is similar to that obtained with the ETS (Figure 4).

2.4. Stress sampling scheme

Keeping in mind that the objective is to feed a seismicity forecast, different sampling strategies of the stress changes might be adopted. A natural choice

would be to sample the stress field at the location where changes are maximum and assuming faults with orientation yielding the maximum Coulomb stress change (Figure 5a) or with a fixed orientation corresponding to one or the other dominant mapped fault orientations (Figure 5b and 5c). These sampling schemes give a disproportionate influence of the very localized areas of faster stress buildup where the reservoir is offset by small faults, as is the case in the southern part of the reservoir, and the stress values are very sensitive to the details of the meshing. In fact, the seismicity does not match particularly well the known faults offsetting the reservoir (Figure 1). A large fraction of the earthquakes thus probably occur on secondary faults that were not mapped and in areas of stress concentration not represented in our reservoir model. We take this as an indication that the reservoir model, although quite detailed, does not account for all the complexity of the reservoir geometry and for the heterogeneities of compressibility responsible for stress build up during reservoir compaction. We however tested these possible sampling schemes as described below and in supplementary figures, and chose as our reference stress model the solution obtained from the more robust scheme by sampling at the cuboid centers (Figure 5d). None of these sampling schemes is completely satisfying to yield a realistic estimate of the stress changes at the exact location of where the earthquakes are induced, but we show below and in supplement that using any of them doesn't impact much the seismicity forecast, essentially because of the model calibration step. In addition, to avoid a seismicity forecast too tightly tied to the particular set of faults represented in the reservoir model, we apply a smoothing to the stress field using a Gaussian kernel with 3.2km standard deviation. This particular value was chosen for consistency with Bourne and Oates (2017) and the resolution of spatial heterogeneities of compressibility. This is an ad hoc way to account for stress concentrations due to secondary faults or to small scale variations of compressibility not represented in our model. This procedure predicts a spatial distribution of earthquakes in better qualitative agreement with the observations than the other sampling schemes that we have tested, including in particular those shown in supplement.

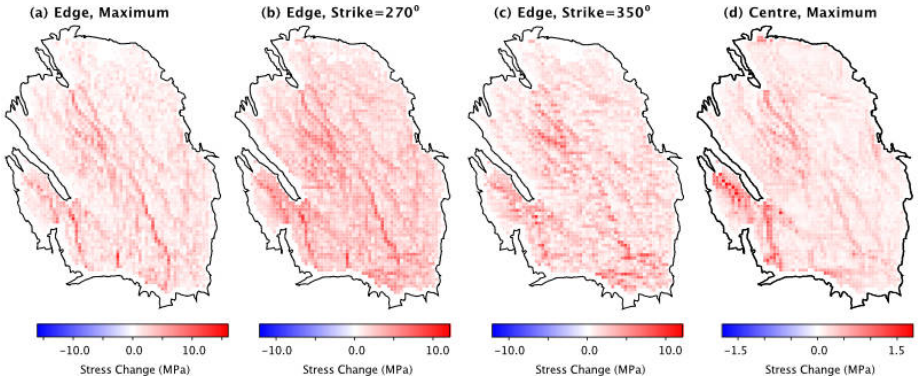

Figure 5: Coulomb stress changes in the caprock, calculated 5m above the reservoir top, between 1965 an 2017. (a) Maximum Coulomb stress change sampled 10m within from the North-East of the cuboid edges. (b) Coulomb stress changes on N270^{o}E striking faults sampled 10m within from the top-right of the cuboid edges.(c) Coulomb stress changes on N350^{o}E striking faults sampled 10m within from the top-right of the cuboid edges. (d) Maximum Coulomb stress change sampled at the center of the cuboids.

We also tested different schemes regarding the depth of the sampling points. Figure 6 shows the stress changes at grid points coinciding in map view with the centers of the cuboids, and at various elevations relative to the reservoir. It illustrates how the maximum Coulomb stress change attenuates away from the zone of stress concentration where the reservoir is offset by faults both in map view and with depth.

We assume that the pore pressure in the domains above and below the reservoir is not connected to the fluid pressure in the reservoir. Figure 6 shows similar patterns of Coulomb stress increase above and below the reservoir. The amplitude of the Coulomb stress change decreases above the reservoir and the spatial distribution evolves slightly, with a Coulomb stress change high in the south-west of the reservoir shifted to the north-east at shallower depth. The variations are small within the top 50m of the reservoir where the distribution of hypocentral depths is peaking (Figure 6). The time-evolution of the maximum Coulomb stress 5m above the reservoir is shown in Supplementary Figure A4.

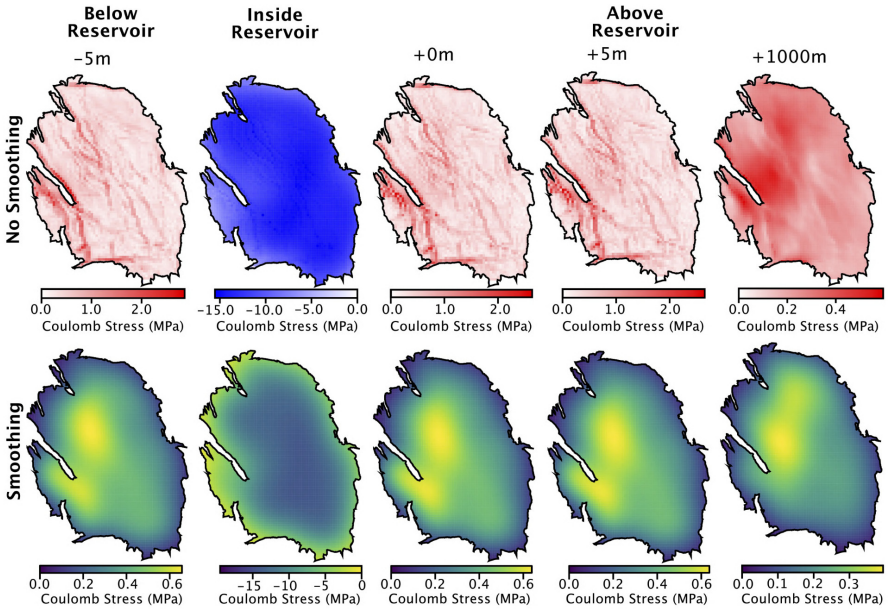

Figure 6: Maximum Coulomb stress changes from 1965 to 2017 at various elevations relative to the reservoir. (a)-(e) represent the maximum Coulomb stress for the unsmoothed. (f)-(j) maximum Coulomb stress models smoothed to a length scale consistent with uniaxial compressibility (3.2km).

Given the similar patterns of stress changes at the various depths, we choose to tie the seismicity to a single reference elevation above the reservoir. This 2-D assumption allows to reduce the computation cost that would be needed for a full 3-D calculation. Given that the depth distribution of hypocenters peaks right above the top of the reservoir, we estimate seismicity rate based on the maximum Coulomb stress change computed 5m above the top of the reservoir with the strain-volume model (Figure 4b; with forecasting potential at different depths and different Coulomb models discussed further in Section 3).

We compare the maximum Coulomb stress change from 1965 to 2017 for the ETS formulation and the maximum Coulomb stress change calculated with our model at 5m above the reservoir (Figure 4). Although the two stress calculation methods significantly differ, the spatial pattern and the amplitudes of Coulomb stress changes are relatively similar.

3. Relating stress changes and seismicity

Stress-based earthquake forecasting requires some scheme to relate induced seismicity to stress changes. Previous Earthquake forecasting studies focused on Groningen have assumed instantaneous failure and a non-critical initial stress (Bourne and Oates, 2017; Bourne et al., 2018; Dempsey and Suckale, 2017), or non-instantaneous failure based on rate-and-state friction (Candela et al., 2019; Richter et al., 2020). In this study we aim at simulating the evolution of seismicity at the annual to multi-annual timescale. In a related study we show that the finite duration of earthquake nucleation doesn't matter at these time scales (Heimisson et al., 2021). We therefore assume here instantaneous failure. Below we test the possibility that the seismicity is consistent the near-exponential rise of seismicity rate due to the tail of the distribution, represented by a generalized Pareto distribution by Bourne et al. (2018), or has transitioned to the steady regime assumed by Dempsey and Suckale (2017).

We use the stress changes calculated from our model and the observed seis-

366 micity to estimate the initial strength excess, defined as the Coulomb stress
367 change needed to bring a fault patch to failure. An earthquake indeed indicates
368 a Coulomb stress change due to gas production equal to the initial strength ex-
369 cess before production started. This calculation requires some knowledge of the
370 fault orientation, which is known only for a very limited number of earthquakes
371 for which focal mechanisms could be calculated (Smith et al., 2020). There-
372 fore, we make the calculation for the fault orientation that yields the maximum
373 Coulomb stress change or the regional fault orientation. Because stress changes
374 are calculated at a reference elevation, samples at the center of the cuboids and
375 smoothed, this distribution does not rigorously represent the strength excess,
376 but can be considered a proxy for it, which we use to estimate of probability of
377 inducing an earthquake at a given stress change. In fact, we can only estimate
378 the part of the initial strength distribution that is revealed by seismicity. The
379 forecast requires a parametric representation of the part of the distribution that
380 has not yet been brought to failure. The shape of that distribution depends
381 in principle on the orientation of the faults and the heterogeneities of the ef-
382 fective stress tensor. For a homogenous tri-axial stress regime and standard
383 Mohr-Coulomb failure criterion, the strength excess can be calculated assuming
384 some distribution of fault orientations. If the activated faults have all the same
385 orientation either because they correspond to a pre-existing tectonic fabric, or
386 are optimally oriented with respect to the stress field, the distributions should
387 be close to a Dirac distribution. In that case all earthquakes would happened
388 at approximately the same Coulomb stress change. Our calculation shows a
389 relatively wide spread of values. The spread of this distribution can result from
390 the heterogeneities of initial effective stress, cohesion, friction, fault orientation,
391 hypocentral depths and from the uncertainties in the stress change calculation.
392 We therefore consider the strength excess as a stochastic variable. This ap-
393 proach is similar to the Extreme threshold Model of Bourne and Oates (2017)
394 which assumes that the seismicity only reflects the tail of the failure probability
395 function (failure of the faults with the smallest strength excess). According to
396 the extreme value theory the tail of the distribution can be represented by a gen-

eralised Pareto distribution (Figure 7) so that the failure probability function becomes

$$P_f = \exp(\theta_1 + \theta_2 \Delta C), \tag{21}$$

where $\theta_1 = \frac{C_t}{\bar{\sigma}}$ and $\theta_2 = \frac{1}{\bar{\sigma}}$ relate to the mean C_t , and standard-deviation $\bar{\sigma}$ of the initial strength excess distribution.

However, it is possible that the seismicity may have transitioned to a more steady regime in which case the representation of only the tail of the distribution might be inadequate. For each fault the distribution of strength excess depends on the probability distributions describing its orientation, stress and strength. Heterogeneities of stress resulting from variations of elastic properties of lithological origin can result in a Gaussian distribution of Coulomb stress changes (Langenbruch and Shapiro, 2014). The other factors of strength excess variability might be assumed, like the geometric effect due to the faults orientation, to be unimodal as well. If we assume that the initial Coulomb stress values on different fault patches are independent and identically distributed random values, then, by virtue of the central limit theorem, we may assume a Gaussian distribution of initial strength excess, as is expected in the case where the only source of strength excess is due to heterogeneities of elastic properties (Langenbruch and Shapiro, 2014). In that case the probability of failure of a fault at a location with a maximum Coulomb stress changes ΔC is derived from integration of the Gaussian function yielding

$$P_f = \frac{1}{2}\left(1 + \operatorname{erf}\left(\frac{\Delta C - \theta_1}{\theta_2\sqrt{2}}\right)\right), \tag{22}$$

where θ_1, θ_2 represent the mean and standard deviation of the Gaussian distribution, representing the fault strength distribution. This formulation is shown by the blue line in Figure 7b, with the initial Gaussian represented by the dashed blue line. As the Coulomb stress increases, the first earthquakes will occur on the faults with the lowest strength excess and so will provide information on the tail of the initial strength excess distribution. In that regime the extreme

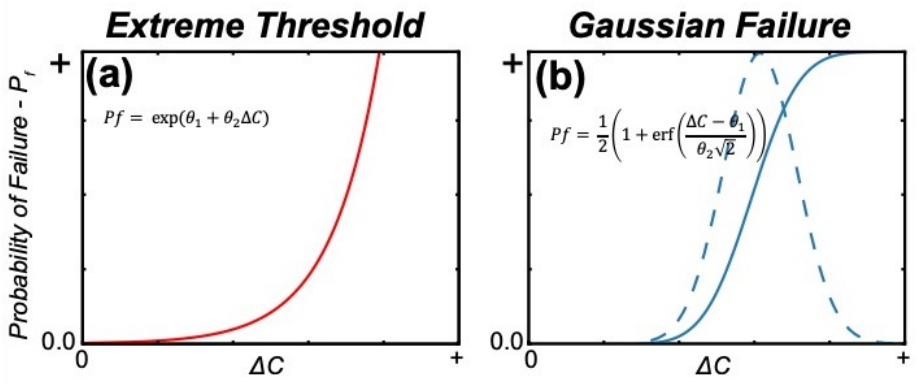

Figure 7: Probabilistic failure functions for the Extreme-Threshold (a) or Gaussian Failure (b) models. The blue dashed line represents the Gaussian distribution and the solid dashed line the cumulative distribution function.

value theory implies an exponential rise of seismicity for a constant stress rate (Bourne and Oates, 2017). As the stress increases to a value of the order of the mean initial strength excess (θ_1) the seismicity rate will gradually evolve to a regime where the seismicity rate will be proportional to the stress rate. If the faults that have already ruptured are allowed to re-rupture and if the Coulomb stress has increased to a value significantly larger than the typical stress drop during an earthquake, the distribution of strength excess will become uniform (constant between 0 and the co-seismic stress drop); the seismicity rate would then remain proportional to the stress rate. This is the steady regime expected an active tectonic setting for instantaneous nucleation (Ader et al., 2014). One important question for seismic hazard assessment at Groningen is whether the system has moved out of the initial exponential rise of seismicity. To address this question, we compare the performance of the Gaussian model describes above, which allows for this transition, and of the Extreme threshold Model of Bourne and Oates (2017) which assumes that the seismicity only reflects the tail of the failure probability function.

Failure Function	θ_1 Bounds	θ_2 Bounds	θ_3 Bounds
Extreme Threshold	$0.0 - 15.0$ MPa	$0.0 - 30.0$ MPa^{-1}	$0.0 - 2.0$
Gaussian Failure	$0.01 - 0.75$ MPa	$0.01 - 0.75$ MPa	$-2.0 - 15$

Table 2: Failure function uniform priors for Extreme Threshold and Gaussian Failure functions.

4. Estimation of model parameters

Here we determine the best fitting failure function parameters relating the modelled Coulomb stress change with the observed regional seismicity. We use the catalogue of Dost et al. (2017) which reports earthquake locations since 1990, with a completeness of $M_{LN} > 1.5$ since 1993. We separate the observed earthquakes into yearly bins, denoted as R_y^o, where subscript y indicates the year and superscript ^{o} stands for "observed". We select a training period $y \in [y_s : y_e]$, where y_s represents the start year of training and y_e is the end year bin. The start year is selected as $y_s = 1990$, where the magnitude of detection is consistently above $M_{LN} = 1.5$ (Dost et al., 2017). The end year is set at 2012 and $2012 - 2017$ is used for validation. The bounds of the uniform prior for the parameter optimisation for the Extreme Threshold and Gaussian failure functions are given in Table 2.

Predicted earthquake rates are formulated using a non-homogeneous Poisson point process with the intensity function represented by:

$$\Lambda = \theta_3 \frac{\partial P_f}{\partial t} \tag{23}$$

where λ represents an earthquake productivity per given volume and $\frac{\partial P_f}{\partial t}$ the partial differential of the probability function changing in time. This formulation contains three unknowns, θ_1, θ_2 and θ_3, which are assumed spatially uniform.

Following Heimisson et al. (2021), we quantify misfit using a Gaussian log-likelihood function. The Poisson Loglikelihood Ogata (1998) is more commonly used. One issue is that it requires a declustered catalog to remove aftershocks. Heimisson Heimisson (2019) shows that Dieterich's model is actually valid even

in presence of inter-event triggering so that it is actually better not to remove aftershocks and that, in that case, a Gaussian Loglikelihood is more adequate. The catalog of Groningen doesn't include much aftershocks apparently, so whether one likelihood or the other is chosen makes no significant difference. The misfit function writes,

$$\log(p(m|R^o)) = -\frac{1}{2}\sum_{i=1990}^{i=2016}\left(R_i^o - \int_\Sigma R(m,i,x,y)dxdy\right)^2, \qquad (24)$$

where $R(m,i)$ is the model predicted rate density in year i, where m is the vector of model parameters. R_i^o is the observed rate in year i. Integration in Easting, x, and Northing y, is carried over the area Σ. because of the predicted seismicity rate can be equal to zero ($R = 0$). During the training we sample the PDF (Equation 24) using an Metropolis-Hastings sampler. After sufficient number of samples, hindcasts are obtained by selecting 1000 random samples of $m = m_1, m_2, \ldots$ at random and computing $R^p(m,t)$ for $t > y_e + 1$.

5. Results and Discussion

In this section we discuss how the observed seismicity compares to model predictions in time and space based on the stress change calculated with strain-volume formulation for the Gaussian and Extreme-Threshold failure functions. We consider predictions based on our reference stress model where the Maximum Coulomb stress changes calculated with the strain-volume formulation at the cuboid centers and smoothed spatially. To simplify the forecast and reduce the comptutaional cost, we relate the seismicity to stress changes calculated 5m above the reservoir top. We also show forecast based on stress changes calculated with the Elastic-Thin-Sheet model and on a variations from our reference model. We show in particular that the forecast is insensitive to the choice of a particular reference depth (Supplementary Figures A4 and A5). We also consider the forecast obtained if no smoothing is applied to the stress field, if stress changes are sampled at the edges of the cuboids where they are maximum, or

if the forecast is based on the Coulomb stress changes on faults with a fixed a orientation set to one or the other of the two dominant orientations observed at Groningen (Supplementary Figures A6, A7 an A8).

5.1. Failure Functions and temporal evolution of seismicity

The observed time-evolution of seismicity is compared to the prediction for the Gaussian and Extreme-Threshold models, using our reference stress model, in Figures 8a and 8c respectively. The differences between the earthquake rates derived from the extreme-threshold and Gaussian failure model are insignificant over the training period. However, we note that the Gaussian model predicts a longer seismicity lag with the onset of seismicity occurring three years after that of the extreme-threshold (Figure 8a and 8b). We verified that given the magnitude-frequency distribution of earthquakes is well described by the Gutenberg-Richter law for a b-value of 1 (Bourne and Oates, 2020), both models are consistent with the fact that no seismicity was reported before 1990 when only earthquakes with magnitude larger than about 2.5 could be detected.

Investigating the temporal forecast across all the model with have tested by varying the sampling location of the stress field and using either the maximum Coulomb stress change or the Coulomb stress change calculated for the average fault orientation, we find little variation in the training logp value. All models perform similarly and also yield similar forecast over the validation period. The validation log-p is however best for the forecast based on the Coulomb stress change calculated 5m above the reservoir (Supplementary Figures A8 and A9).

Figure 9 shows the distribution of Coulomb stress changes calculated at the earthquake location for comparison with the failure functions obtained from our inversion. The comparison shows that even with the Gaussian model the seismicity data constrain mostly the tail of the distribution. Some of the acceptable Gaussian models show a roll-over that would suggest the beginning of the transition to a more steady regime. In any case, the two model parametrizations

yield relatively similar failure function in the domain constrained by the observations. These distributions depend on the input stress field and so the actual values of the stresses would be rescaled if another stress field is chosen as an input. A key point is that the introduction of a stress threshold provides a sound way to explain the lag of the seismicity response to the gas extraction. Another key point is that the stochastic distribution of this threshold can explain well the initially exponential rise of seismicity as initially suggested by Bourne et al. (2018). An alternative representation, presented in Heimisson et al. (2021), is to assume a population of faults below steady-state with nucleation governed by rate and state friction. In that case, a single stress threshold is introduced, which estimated to 0.17MPa with a 95% of $0.07 - 0.18$MPa using the same reference stress model as in this study. For comparison, we get a threshold distribution peaking at 0.32MPa with a standard deviation of 0.07MPa. The two notions are however not equivalent as the threshold associated to the rate-and-state model of nucleation determines the stress needed for a fault patch to evolve toward rupture, while our Gaussian failure model assumes instantaneous nucleation. The distribution of the initial state variable determines the time distribution of earthquakes in the rate and state model.

5.2. Spatial distribution of seismicity

We compare here the spatial distribution of earthquake probability predicted by our models to the observed seismicity. We test the strain-volume and thin-sheet stress redistribution models, and the extreme-threshold and Gaussian failure models, leading to four predictions. Figure 10 shows the observed and predicted seismicity for various models in addition to our reference model. All these model were calibrated against the observations. We show only the prediction from the best-fitting set of parameters.

The Gaussian and extreme-threshold failure models predicts similar spatial distribution of earthquake probability, whether the strain-volume or thin-sheet formulations is chosen to calculate stress redistribution. Slight differences are visible though. For the thin-sheet formulation the Gaussian failure function

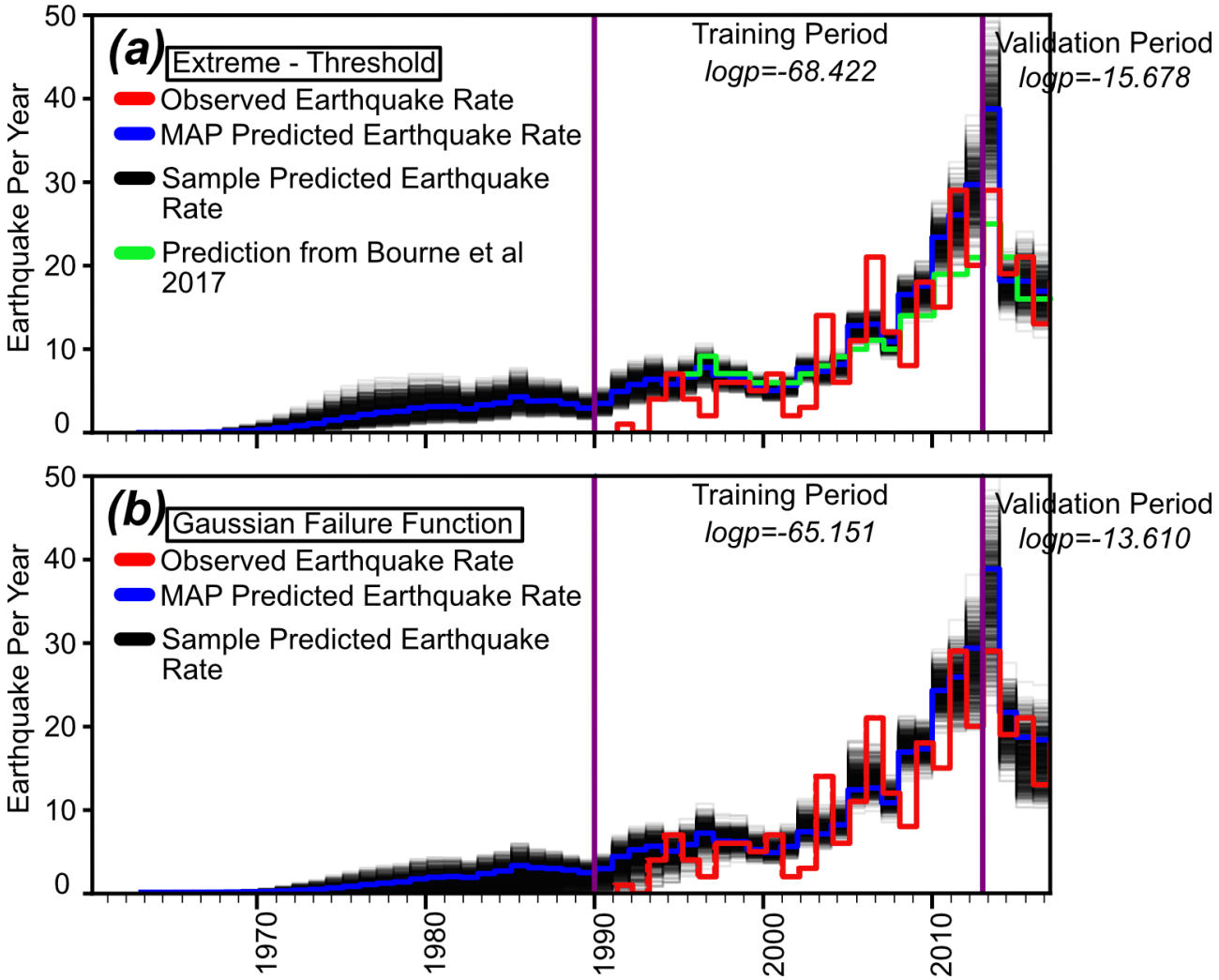

Figure 8: Comparisons of the observed seismicity rate with predicted rates calculated with the extreme-threshold (a) and Gaussian (b) failure models using the strain-volume formulation. Blue lines represent the maximum a posteriori (MAP) estimate of earthquake rate. Grey shading represents the probability distribution. Red solid line represents the observed seismicity catalogue used for training. The green line in panel (a) represents the best fitting prediction based on the thin-sheet approximation and extreme threshold model (Bourne and Oates, 2017).

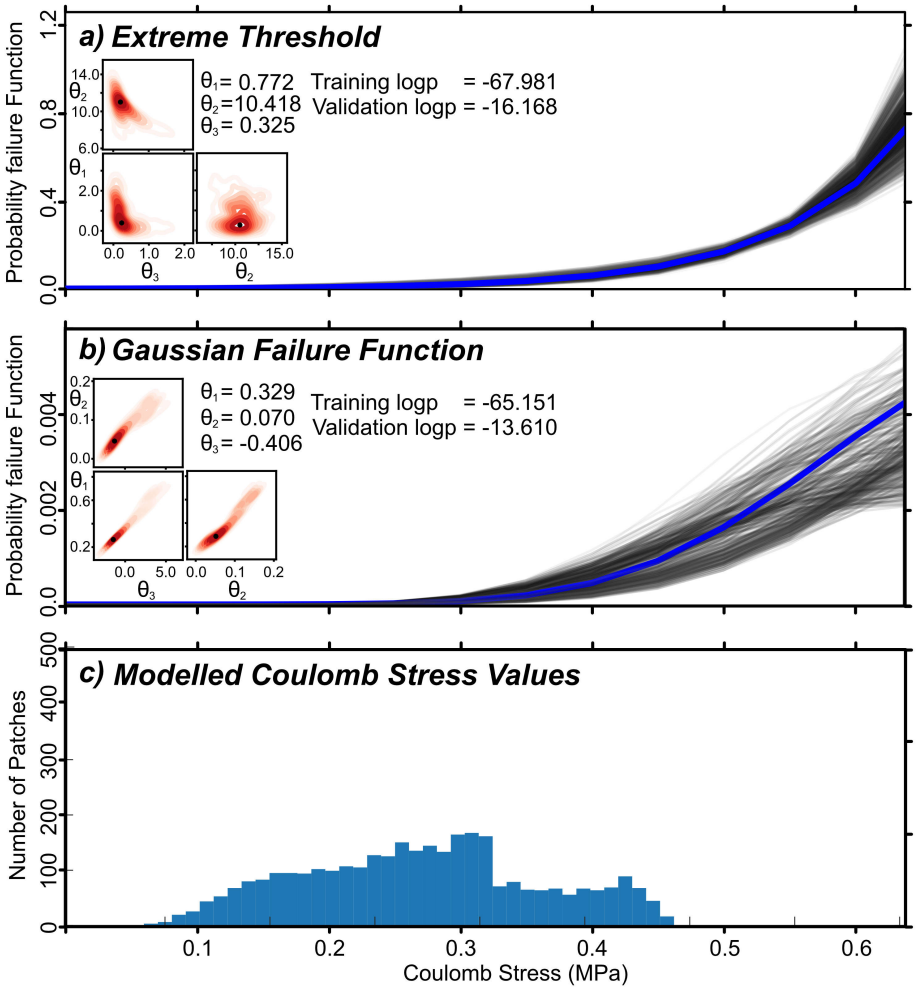

Figure 9: Optimised probability failure functions for the extreme-threshold and Gaussian failure functions. Blue lines represent the maximum a priori estimate of synthetic earthquake rate. Black lines represent samples from the probability distribution with colour dependent on the probability. (a) Extreme threshold failure function. (b) Gaussian failure function. (c) Histogram of the modelled Coulomb stress values across the reservoir from the strain-volume formulation.

yields higher probability of failure in the north-west of the reservoir region compared to the extreme-threshold failure criterion. When the the input stress field is not smoothed and sampled either at the cuboid centers or at the cuboid edges where stress changes are maximum, the forecast in time is good (Figure A7), although with p-values not as good as what can obtained with the smoothed stress field. They however make distinct predictions regarding the spatial distribution of earthquakes (Figure A7). They predict a very heterogenous spatial distributions that don't match well the observed seismicity (Figure 10). Because of the small catalog, we didn't carry out statistical tests, but we don't think would be appropriate to use such models for hazard assessment because there is no indication that the spatial heterogeneities predicted by those models are valid.

It should be noted that the best-fitting model parameters are significantly different depending on the choice of the input stress field and reference elevation. The Coulomb stress changes at the location of the EQs are probably underestimated in our reference model. This bias is compensated by the calibration of the model parameters against the observed seismicity. The procedure has merit for the purpose of probabilistic seismicity forecasting but the model parameters are biased.

5.3. Are earthquake nucleating in the caprock, reservoir or underburden?

The model accounts for stress redistribution withing and outside the reservoir with account for stress localization at the faults offsetting the reservoir. The importance of accounting for this process has been demonstrated in a number of previous studies (Mulders, 2003; Rutqvist et al., 2016; Buijze et al., 2017, 2019; Jansen et al., 2019). In agreement with these studies, we find that the stress changes are maximum at the top or bottom of the reservoir in the vicinity of discontinuities created by faults offsetting the reservoir due to faulting. The model is consistent with the observation that seismicity hypocenters tend to concentrate in the caprock. The seismic ruptures don't need to be confined

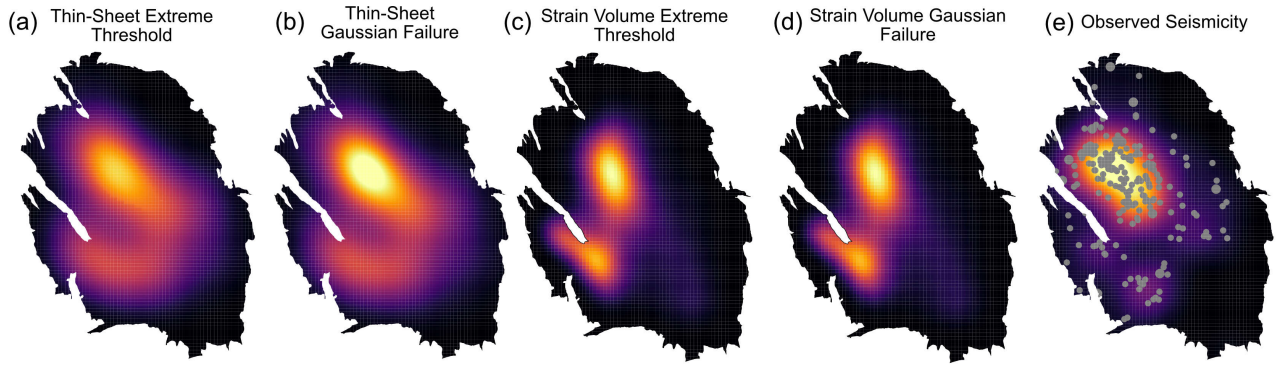

Figure 10: Spatial distribution of earthquake probability for various models compared to observed seismicity. (a) Observed seismicity during the $1993 - 2012$ training period (white dots), with shading showing the normalized density of earthquakes obtained by convolution with a Gaussian kernel with a 3.2 km standard deviation. (b) Model prediction using the reference stress model (maximum Coulomb stress change sampled at cuboid centers, 5m above the top of the reservoir smoothed with a Gaussian kernel of 3.2 km standard deviation) and the Gaussian failure function.(c) Same as (a) using the extreme threshold failure function. (d) Model prediction using the Elastic-Thin-sheet formulation and extreme threshold failure model. (e) Elastic-Thin-sheet stress formulation using Gaussian failure function.(f) Same as (a) using the unsmoothed version of the reference model. (g) Model prediction using maximum Coulomb stress change sampled at the cuboid centers with no-smoothing and the Gaussian failure function (h) Same as (e) for Coulomb stress change on N270E striking faults

to the caprock though, are they can expand both into the reservoir or into the overburden.

This view contrast with a number of previous studies (Dempsey and Suckale, 2017; Bourne and Oates, 2017; Richter et al., 2020) which have assumed that earthquakes were triggered within the reservoir due to poroelasticity.The seismicity data don't exclude that the earthquakes might nucleate within the reservoir. In that regard, it should be noted that our reference model predicts no Coulomb stress increase in the reservoir due to the choice of standard mechanical properties (Poisson coefficient of 0.25, Friction of 0.66, and Biot coefficient 1.0). Our model can however predict an increase of Coulomb stress in the reservoir for still realistic model parameters ($\alpha > \alpha_c = \frac{1-\nu}{1-2\nu}\frac{2\sin\phi}{1+\sin\phi}$). This condition is not strict however as it ignores the effect of the finite extent of the reservoir and spatial variation of its geometry. Most importantly we find that, once the model parameters are calibrated to fit the observations, the forecast is nearly identical whether the earthquakes are assumed to nucleate within or outside the reservoir.

The seismicity data make it improbable that earthquakes below the reservoir. Our model doesn't provide any explanation for this observation as it predicts a similar stress concentration in the overbuden and underburden. Stress changes are actually slightly smaller in the underburden because of the asymmetry induced by the free surface. One possible explanation would be that the fluid pressure in the underburden is more connected to the reservoir than in the caprock, which has obviously been an effective seal over geological time. This explanation is plausible because the Carboniferous shale-Slitstone formation in the underbuden is actually the source of the gas that has accumulated in the Slochteren reservoir sandstone. In that case the Coulomb stress might have actually dropped in the underburden leading to fault stabilization. Another possibility is that faults in the underburden had a larger initial strength excess due to the larger lithostatic pressure (as in Buijze et al. (2019)), or to stress relaxation associated wih dusctile flow of the shale. Finally, it is possible also that the shale and siltstone below the reservoir are less seismogenic than the an-

hydrite caprock. Laboratory measurements show no evidence that earthquake cannot nucleate in the underburden, although they point to a larger strength drop in the caprock that would be more favorable to earthquake nucleation there (Hunfeld et al., 2021) .

6. Conclusions

This manuscript presents a framework for stress-based earthquake forecasting of induced seismicity which should in principle be applicable in any setting where earthquake are induced by deformation of a reservoir whether due to extraction or injection. The framework requires some knowledge of the reservoir geometry and compressibility on one hand, and of the pore pressure evolution on the other hand. By representing the reservoir as a series of poroelastic cuboids, the stress redistribution withing and outside the reservoir can calculated with proper account for stress localization at the faults offsetting the reservoir and poroelastic effects.The stress changes are calculated using semi-analytical Green functions. This procedure is computationally very efficient and can therefore be applied to compute stress changes at the scale of the entire reservoir over several decades with a sub-kilometric spatial sampling rate and a yearly temporal resolution. We use our method to calculate stress changes due to the reservoir compaction to feed an earthquake forecasting scheme. Our scheme is similar to but expands on the extreme threshold model of Bourne and Oates (2017); Bourne et al. (2018) by allowing in principle to represent the transition from the initial exponential rise of seismicity to the steady state regime where the seismicity rate should be proportional to the stress rate. We find that the Gaussian failure function, which we introduce to that effect, has in fact an only slightly lower validation loss than the extreme-threshold function. We find no evidence that the seismicity at Groningen has actually transitioned to the steady-state regime. Assuming a steady state regime therefore probably lead to an underestimation of the hazard level.

We find that the forecasting performance is similar if the stress calculation is

based on the elastic thin sheet approximation (Bourne and Oates, 2017) or on the strain-volume method presented here. It is also independent of the chosen vertical distance from the top of the reservoir used to extract the stress changes. This is due to the fact that, in all these cases, the seismicity forecast is driven by the spatial distribution of the discontinuities of the reservoir and the time evolution by the pressure depletion history. The forecasting procedure seems therefore relatively robust to the uncertainties on the modeling assumptions. However, it is likely the forecast performance is satisfying because the seismicity has been relatively stationary. If seismicity had shifted to the underburden for example, it is probable that the forecasting performance of the algorithm would drop and that the model parameters would need to be reevaluated. In any case, one should be cautious about the interpretation of the model parameters and about the implications of a satisfying forecast. For example, the stress threshold needed to initiate seismicity in our model depends on the chosen elevation above the reservoir where the stresses are calculated and on the scheme used to sample stress changes or evaluate earthquake probabilities. A satisfying forecast doesn't mean that the particular choices made in the stress calculation or the failure functions are correct. As an example a forecast based on the assumption that the earthquakes initiate in the reservoir can be found satisfying, although the assumption might be incorrect. Similarly, the assumption of a steady regime might seem acceptable to forecast seismicity over a short period of time but the linear extrapolation that the assumption implies could be incorrect and the model parameters (the ratio between the stress rate and the seismicity rate) would be dependent on the period used to calibrate the model and would have little physical significance.

The procedures presented in this article is computationally effective and could be implemented into a traffic-light system during reservoir operations. It would also easily allow for data assimilation (re-evaluation of the model parameters as seismicity observations are collected).

In this work we have assumed that earthquakes nucleate instantaneously at a critical stress. We do not account for the finite duration of the nucleation process

which can be described using the rate-and-state friction formalism and which has been used in some previous studies and could partly explain the seismicity lag at Groningen (Candela et al., 2019; Richter et al., 2020). These studies use the Dieterich (1994) model, that the earthquake population is at state of steady earthquake production before it is perturbed. This hypothesis therefore ignores that the system may have been initially in a relaxed state due to the low level of tectonic loading in the Groningen context. Some modification of the formalism, presented in Heimisson et al. (2021), is needed to account for a possible initial strength excess. Although we didn't presented any such simulations here, the code supplied in the Google Colab notebook include the possibility of running forecast with the threshold rate-and-state model (Heimisson et al., 2021).

Acknowledgments

This study was supported by the NSF/ IUCRC Geomechanics and Mitigation of Geohazards (National Science Foundation award 1822214). We gratefully acknowledge data and support from Nederlandse Aardoli Maatschappij (Jan van Elk, Gini Ketelaar), Shell Global Solutions (Stijn Bierman, Steve Oates and Xander Campman) and Koninkljjk Nederlands Meteorologisch Instituut (http://www.knmi.nl/). Strain Volume simulations can be found at the interactive Google Colab notebook `https://colab.research.google.com/drive/1GDKMHDO2obj4bT8ezvCxFumHz3CSE3Ns?usp=sharing`.

Contributions

J.D.Smith: Model method conceptualization, software development and manuscript writing. E.R.Heimisson: Software development and manuscript writing. S.J.Bourne: Supervision, Model method conceptualization, software development. JP.Avouac: Supervision, Model method conceptualization and manuscript writing.

References

Ader, T.J., Lapusta, N., Avouac, J.P., Ampuero, J.P., 2014. Response of rate-and-state seismogenic faults to harmonic shear-stress perturbations. Geophysical Journal International 198, 385–413.

Bourne, S., Oates, S., Van Elk, J., 2018. The exponential rise of induced seismicity with increasing stress levels in the groningen gas field and its implications for controlling seismic risk. Geophysical Journal International 213, 1693–1700.

Bourne, S.J., Oates, S.J., 2017. Extreme threshold failures within a heterogeneous elastic thin sheet and the spatial-temporal development of induced seismicity within the groningen gas field. Journal of Geophysical Research: Solid Earth 122, 10,299–10,320. URL: https://agupubs.onlinelibrary.wiley.com/doi/abs/10.1002/2017JB014356, doi:10.1002/2017JB014356, arXiv:https://agupubs.onlinelibrary.wiley.com/doi/pdf/10.1002/2017JB014356.

Bourne, S.J., Oates, S.J., 2020. Stress-dependent magnitudes of induced earthquakes in the Groningen gas field. Journal of Geophysical Research: Solid Earth 125, e2020JB020013. doi:https://doi.org/10.1029/2020JB020013.

Buijze, L., Van den Bogert, P., Wassing, B., Orlic, B., 2019. Nucleation and arrest of dynamic rupture induced by reservoir depletion. Journal of Geophysical Research: Solid Earth 124, 3620–3645.

Buijze, L., Van Den Bogert, P.A., Wassing, B.B., Orlic, B., Ten Veen, J., 2017. Fault reactivation mechanisms and dynamic rupture modelling of depletion-induced seismic events in a rotliegend gas reservoir. Netherlands Journal of Geosciences 96, s131–s148.

Candela, T., Osinga, S., Ampuero, J.P., Wassing, B., Pluymaekers, M., Fokker, P.A., van Wees, J.D., de Waal, H.A., Muntendam-Bos, A.G., 2019. Depletion-induced seismicity at the groningen gas field: Coulomb rate-and-state models including differential compaction effect. Journal of Geophysical Research: Solid Earth 124, 7081–7104.

Dempsey, D., Suckale, J., 2017. Physics-based forecasting of induced seismicity at groningen gas field, the netherlands. Geophysical Research Letters 44, 7773–7782.

Dieterich, J., 1994. A constitutive law for rate of earthquake production and its application to earthquake clustering. Journal of Geophysical Research: Solid Earth 99, 2601–2618. doi:https://doi.org/10.1029/93JB02581.

Dost, B., Ruigrok, E., Spetzler, J., 2017. Development of seismicity and probabilistic hazard assessment for the groningen gas field. Netherlands Journal of Geosciences 96, s235–s245.

Dost, B., van Stiphout, A., Kühn, D., Kortekaas, M., Ruigrok, E., Heimann, S., 2020. Probabilistic moment tensor inversion for hydrocarbon-induced seismicity in the groningen gas field, the netherlands, part 2: Application. Bulletin of the Seismological Society of America 110, 2112–2123.

Dyskin, A.V., Pasternak, E., Shapiro, S.A., 2020. Fracture mechanics approach to the problem of subsidence induced by resource extraction. Engineering Fracture Mechanics 236, 107173.

Geertsma, J., 1973. Land subsidence above compacting oil and gas reservoirs. Journal of petroleum technology 25, 734–744.

Handin, J., 1969. On the coulomb-mohr failure criterion. Journal of Geophysical Research 74, 5343–5348.

Heimisson, E.R., 2019. Constitutive law for earthquake production based on rate-and-state friction: Theory and application of interacting sources. Journal of Geophysical Research: Solid Earth 124, 1802–1821. doi:10.1029/2018JB016823.

Heimisson, E.R., Smith, J.D., Avouac, J.P., Bourne, S.J., 2021. Coulomb threshold rate-and-state model for fault reactivation: application to induced seismicity at Groningen. Geophysical Journal International 228, 2061–2072. doi:10.1093/gji/ggab467.

Hettema, M., Schutjens, P., Verboom, B., Gussinklo, H., 2000. Production-induced compaction of a sandstone reservoir: the strong influence of stress path. SPE Reservoir Evaluation & Engineering 3, 342–347.

Hol, S., van der Linden, A., Bierman, S., Marcelis, F., Makurat, A., 2018. Rock physical controls on production-induced compaction in the groningen field. Scientific reports 8, 1–13.

Hunfeld, L.B., Chen, J., Niemeijer, A.R., Ma, S., Spiers, C.J., 2021. Seismic slip-pulse experiments simulate induced earthquake rupture in the groningen gas field. Geophysical Research Letters 48, e2021GL092417. doi:https://doi.org/10.1029/2021GL092417.

Jansen, J., Singhal, P., Vossepoel, F., 2019. Insights from closed-form expressions for injection-and production-induced stresses in displaced faults. Journal of Geophysical Research: Solid Earth 124, 7193–7212.

King, G.C., Stein, R.S., Lin, J., 1994. Static stress changes and the triggering of earthquakes. Bulletin of the Seismological Society of America 84, 935–953.

Kuvshinov, B.N., 2007. Reflectivity method for geomechanical equilibria. Geophysical Journal International 170, 567–579.

Kuvshinov, B.N., 2008. Elastic and piezoelectric fields due to polyhedral inclusions. International Journal of Solids and Structures 45, 1352–1384.

Langenbruch, C., Shapiro, S.A., 2014. Gutenberg-richter relation originates from coulomb stress fluctuations caused by elastic rock heterogeneity. Journal of Geophysical Research: Solid Earth 119, 1220–1234. URL: https://agupubs.onlinelibrary.wiley.com/doi/abs/10.1002/2013JB010282, doi:https://doi.org/10.1002/2013JB010282, arXiv:https://agupubs.onlinelibrary.wiley.com/doi/pdf/10.1002/2013JB010282.

van der Molen, J., Peters, E., Jedari-Eyvazi, F., van Gessel, S.F., 2019. Dual hydrocarbon–geothermal energy exploitation: potential synergy between the

production of natural gas and warm water from the subsurface. Netherlands Journal of Geosciences 98.

Mulders, F.M.M., 2003. Modelling of stress development and fault slip in and around a producing gas reservoir. Doctoral Thesis .

Nederlandse Aardolie Maatschappij, 2013. A technical addendum to the winningsplan groningen 2013 subsidence, induced earthquakes and seismic hazard analysis in the groningen field. NAM, Assen .

Ogata, Y., 1998. Space-time point-process models for earthquake occurrences. Annals of the Institute of Statistical Mathematics 50, 379–402. doi:10.1023/A:1003403601725.

Richter, G., Sebastian, H., Torsten, D., Gert, Z., 2020. Stress-based, statistical modeling of the induced seismicity at the groningen gas field, the netherlands. Environmental Earth Sciences 79.

Rutqvist, J., Rinaldi, A.P., Cappa, F., Jeanne, P., Mazzoldi, A., Urpi, L., Guglielmi, Y., Vilarrasa, V., 2016. Fault activation and induced seismicity in geological carbon storage–lessons learned from recent modeling studies. Journal of Rock Mechanics and Geotechnical Engineering 8, 789–804.

Smith, J.D., Avouac, J.P., White, R.S., Copley, A., Gualandi, A., Bourne, S., 2019. Reconciling the long-term relationship between reservoir pore pressure depletion and compaction in the groningen region. Journal of Geophysical Research: Solid Earth 124, 6165–6178. URL: https://agupubs.onlinelibrary.wiley.com/doi/abs/10.1029/2018JB016801, doi:10.1029/2018JB016801, arXiv:https://agupubs.onlinelibrary.wiley.com/doi/pdf/10.1029/2018JB016801.

Smith, J.D., White, R.S., Avouac, J.P., Bourne, S., 2020. Probabilistic earthquake locations of induced seismicity in the groningen region, the netherlands. Geophysical Journal International 222, 507–516.

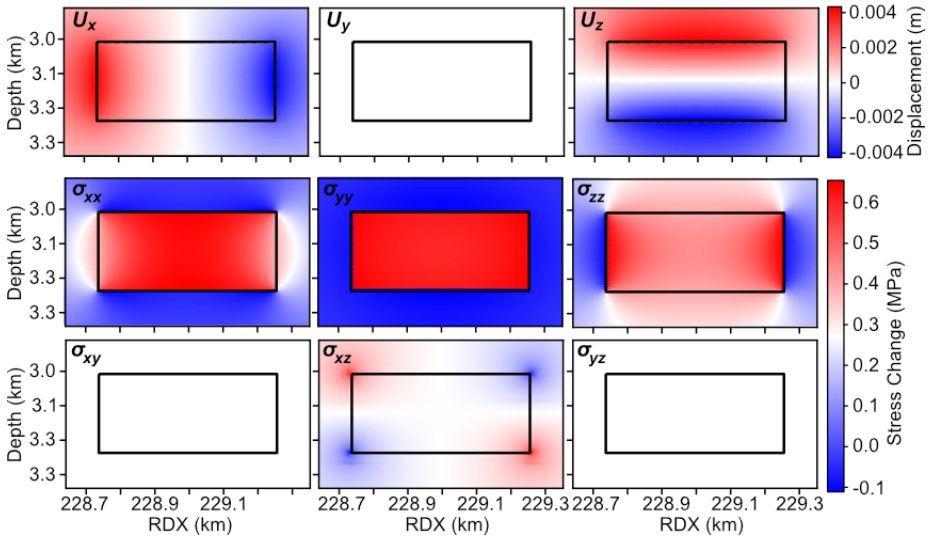

Figure A1: Displacement and stress changes induced by a single cuboid. The position and width of the cuboid is [228.5 km RDX, 574.5 km RDX, 3.018 km Depth] and [500 m, 500 m, 216 m]. The pressure depletion and uniaxial compressibility is 3.3 MPa and 1.816×10^{-11}

Wang, H., 2018. Introduction to poroelasticity .

van Wees, J.D., Pluymaekers, M., Osinga, S., Fokker, P., Van Thienen-Visser, K., Orlic, B., Wassing, B., Hegen, D., Candela, T., 2019. 3-d mechanical analysis of complex reservoirs: a novel mesh-free approach. Geophysical Journal International 219, 1118–1130.

Figure A5

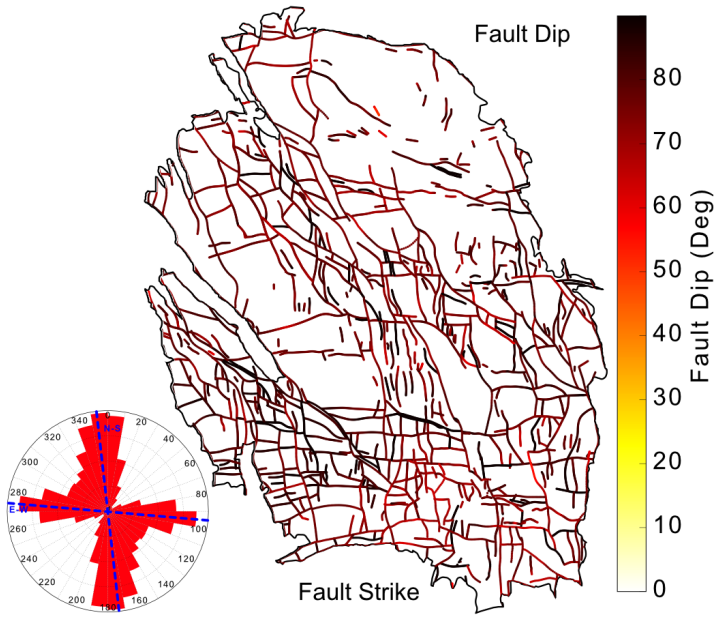

Figure A2: Map of faults offsetting the reservoir, color-coded with estimated dip angle (right). Rose diagram in inset shows the distribution of fault strike. Information on faults taken from Nederlandse Aardolie Maatschappij (2013).

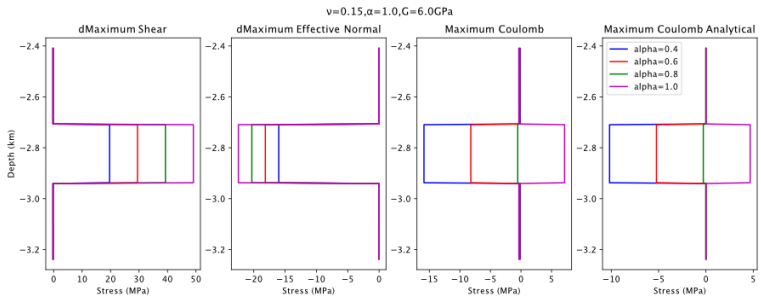

Figure A3: Stress changes calculated at the center of a reservoir of large spacial extent (a cuboid of 230m thickness and $38.5km \times 38.5$km extent) at 2.94km depth, submitted to a pressure drop of 19.5MPa. The same values of the Poisson and friction coefficients ($\nu = 0.15$, $\mu = 0.66$) are used as in the nominal simulations shown in the main text, but the Biot coefficient is varied. In that case the maximum Coulomb stress is positive if the Biot coefficient exceeds a critical value. For a reservoir of infinite extent the critical value is $\alpha_c = 0.84$ (Equation 17). The ratio of the Coulomb stress change to the pore pressure change is $\frac{\Delta C}{\Delta P} = 2(1 - \frac{alpha}{\alpha_c})\sin\phi$, where ϕ is the friction angle ($\tan\phi = \mu$). This analytical prediction is shown for comparison withe the model output in the right panel.

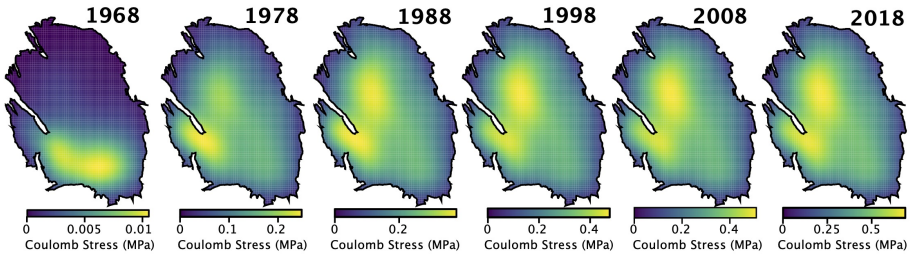

Figure A4: Time evolution of maximum Coulomb stress change calculated 5m above the top of the reservoir and smoothed with a Gaussian kernel with 3.2km standard deviation.

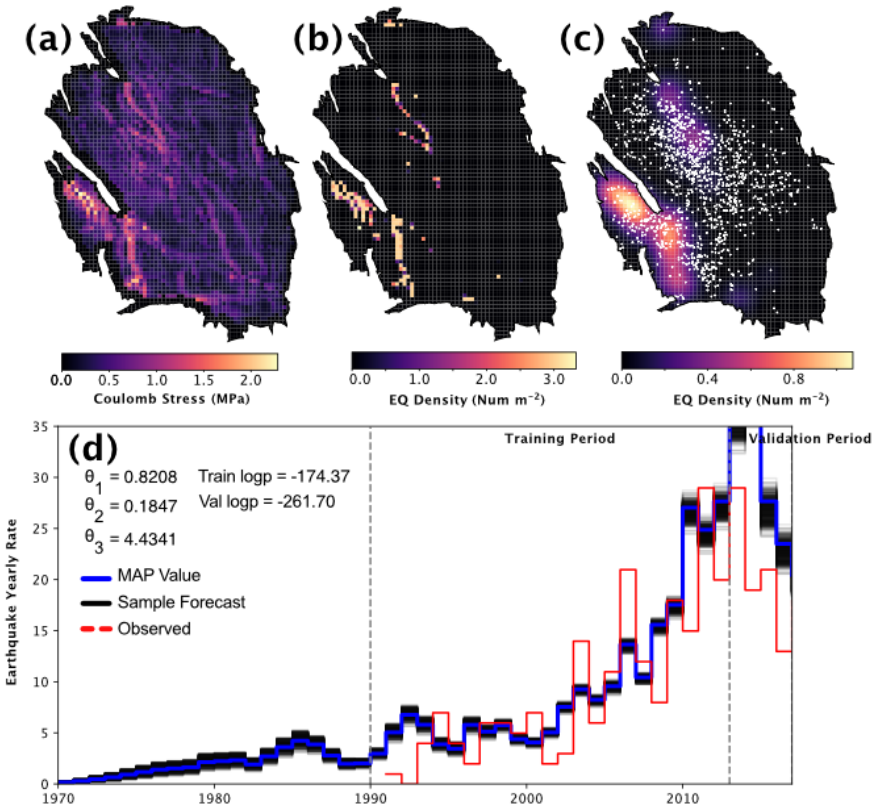

Figure A5: Temporal and spatial variations of seismicity rate predicted based on the maximum Coulomb stress changes on $N270\,\mathrm{deg}\,E$ striking and 80 deg dipping faults calculated 5 m above the reservoir at the midpoint of the cuboid edges. No smoothing was applied. (a) Map of Coulomb stress change. (b) Spatial distribution of forecast seismicity. (c) Observed seismicity (white dots) and predicted spatial distribution of seismicity rate smoothed using a Gaussian filter with 3km standard deviation. (d)Comparison of predicted and observed temporal variation of seismicity rate. The best fitting model parameters and the loglikelihood p-values for the training and validation periods are listed in panel d.

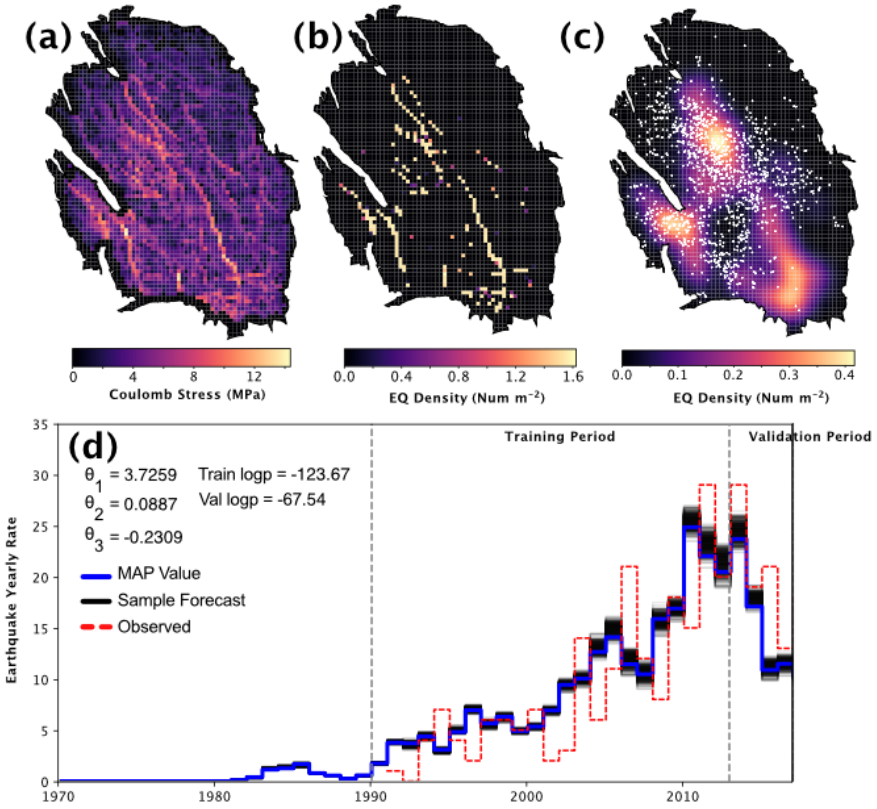

Figure A6: Temporal and spatial variations of seismicity rate predicted based on the Coulomb stress changes on $N270\,\mathrm{deg}\,E$ striking and 80 deg dipping faults calculated 5 m above the reservoir 10m within the North-East corner of the cell. (a) Map of Coulomb stress change with no smoothing. (b) Spatial distribution of forecast seismicity based on panel a. (c) Observed seismicity (white dots) and predicted spatial distribution of seismicity rate smoothed using a Gaussian filter with 3km standard deviation. (d)Comparison of predicted and observed temporal variation of seismicity rate. The best fitting model parameters and the loglikelihood p-values for the training and validation periods are listed in panel d.

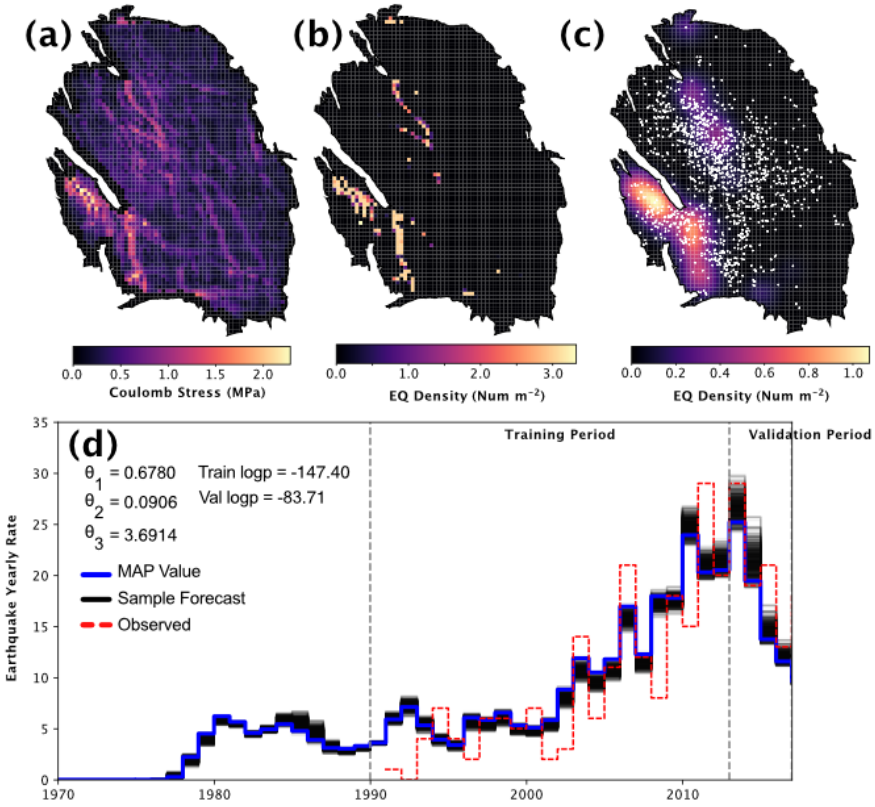

Figure A7: Temporal and spatial variations of seismicity rate predicted based on the Coulomb stress changes on $N350\,\mathrm{deg}\,E$ striking and 80 deg dipping faults calculated at an elevation of 5 m above the reservoir at the cuboid centers. (a) Map of Coulomb stress change with no smoothing. (b) Spatial distribution of forecast seismicity based on panel a. (c) Observed seismicity (white dots) and predicted spatial distribution of seismicity rate smoothed using a Gaussian filter with 3km standard deviation. (d)Comparison of predicted and observed temporal variation of seismicity rate. The best fitting model parameters and the loglikelihood p-values for the training and validation periods are listed in panel d.

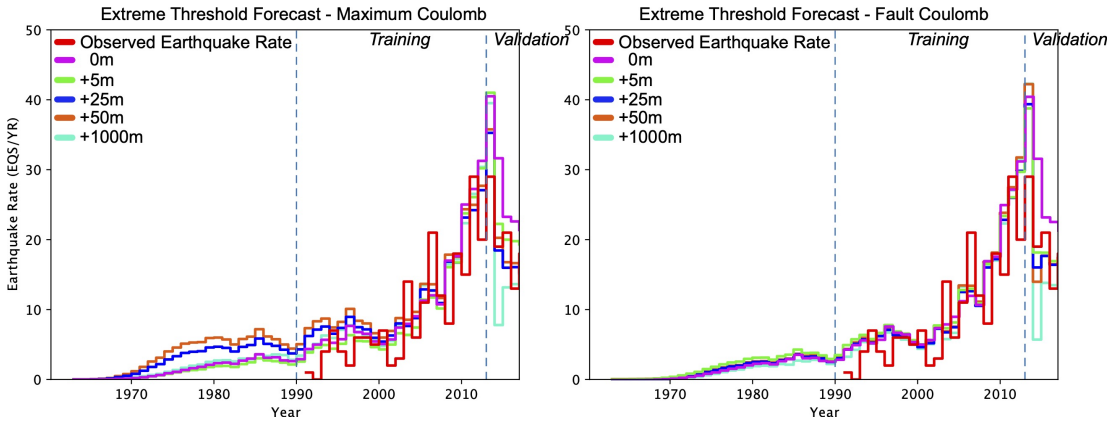

Figure A8: Predicted earthquake rates at different depths for the Extreme Threshold failure criterion and based on the smoothed distribution stress changes calculated at the cuboid centers. Left panel: maximum Coulomb stress change. Right panel: Coulomb stress change on $N350\,\mathrm{deg}\,E$ striking and 80 deg dipping faults.

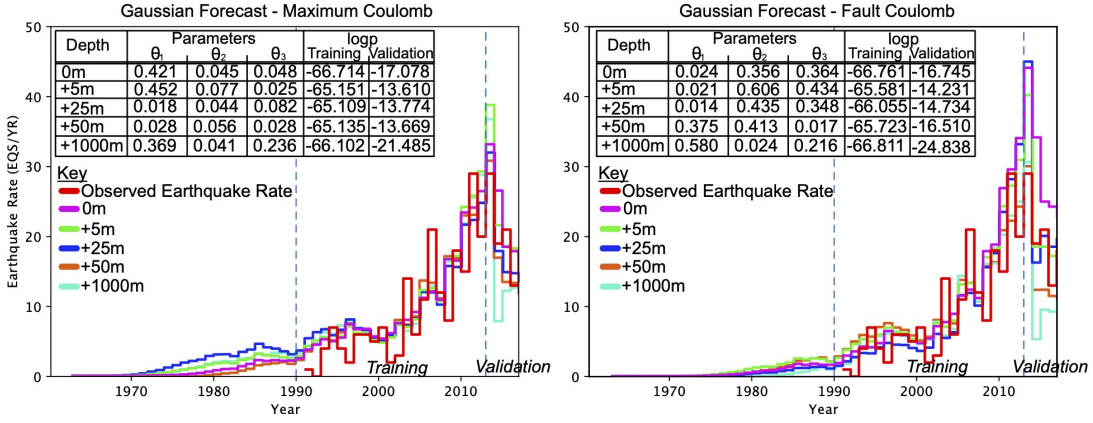

Figure A9: Predicted earthquake rates at different depths for the the Gaussian failure criterion and based on the smoothed distribution stress changes calculated at the cuboid centers. Left panel: maximum Coulomb stress change. Right panel: Coulomb stress change on $N350\,\mathrm{deg}\,E$ striking and 80 deg dipping faults.